ACS OMEGA

Open Access

http://pubs.acs.org/journal/acsodf

Article

High Capacity NbS_2-Based Anodes for Li-Ion Batteries

Alexandra Carvalho,* Vivek Nair, Sergio G. Echeverrigaray,* and Antonio H. Castro Neto

Cite This: *ACS Omega* 2024, 9, 33912−33918

Read Online

ACCESS | Metrics & More | Article Recommendations

ABSTRACT: We have investigated the lithium capacity of the 2*H* phase of niobium sulfide (NbS_2) using density functional theory calculations and experiments. Theoretically, this material is found to allow the intercalation of a double layer of Li in between each NbS_2 layer when in equilibrium with metal Li. The resulting specific capacity (340.8 mAh/g for the pristine material, 681.6 mAh/g for oxidized material) can reach more than double the specific capacity of graphite anodes. The presence of various defects leads to an even higher capacity with a partially reversible conversion of the material, indicating that the performance of the anodes is robust with respect to the presence of defects. Experiments in battery prototypes with NbS_2-based anodes find a first specific capacity of about 1,130 mAh/g, exceeding the theoretical predictions.

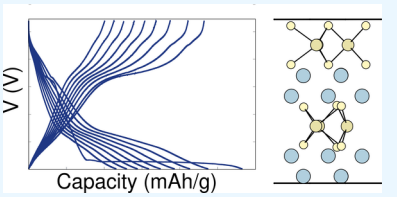

1. INTRODUCTION

Mobile technologies have become an increasingly pervasive part of daily life, and have led to an insatiable consumer demand for smaller, higher-capacity, fast-charging batteries. Concurrently, vehicle electrification is driving a demand for batteries that allow for a longer vehicle range, but at the same time have a longer lifespan (cyclability), and are safer and environmentally friendly.

Currently, most of the existing Li-ion batteries use an intercalation-type anode material like graphite. Graphite provides a specific capacity of 372 mAh/g[1] but presents various problems like dendrite formation and plating which cause irreversible capacity loss and safety hazards.[2] It is expected that an improvement of the energy density of automotive cells above 260 Wh/kg ceiling can be achieved by pairing up layered nickel-rich ternary cathode materials with either Si-containing anodes[3] or Li-metal anodes.[4] However, these anodes also present stability issues. Li metal has the highest theoretical Li packing density, but when it is used as an anode, it undergoes platting/stripping[5] while the cathode undergoes intercalation/deintercalation (in the case of insertion compounds) or conversion reactions (in the case of the sulfur cathode). This results in capacity loss, dendrite formation, and stability issues. Silicon anodes have a theoretical Li capacity of about 4200 mAh/g, being able to store 4.4 Li ions per original Si atom ($Li_{22}Si_5$) when fully lithiated,[6,7] not by intercalation, but through a "conversion" mechanism, where silicon and lithium ions form an electrochemical alloy, breaking/restoring bonds during charge/discharge cycling. Since the bonds established in the alloy are much stronger than the typical electrostatic and van der Waals attraction between the Li ions and intercalation hosts, there is irreversible damage during the charge/discharge cycle, and therefore attaining Si anode cyclability is much more problematic.[8,9] Another major challenge with silicon anodes is that they typically expand by up to 300% of their original volume during lithiation. This swelling can lead to mechanical stresses and fractures in the anode material, which can cause capacity loss and reduced cycle life of the battery, and has so far prevented widespread adoption of pure silicon as an anode material. Various strategies have been investigated to mitigate this issue. Using nanostructured silicon materials, it is possible to cushion the expansion and prevent stress fracture and pulverization,[10−13] but damage still occurs at the silicon surface, affecting the solid electrolyte interphase (SEI) and leading to capacity fade.[8] To use silicon to boost capacity while avoiding these challenges, manufacturers add less than 10% silicon or silicon oxide to graphite anodes.[3,14] It is therefore desirable to find anode materials that have high capacity but without the accompanying volume expansion that is problematic in silicon anodes, either to use as main anode material or as an additive.

Transition metal dichalcogenides can host intercalated Li, similar to graphite.[15] However, conversion-type reactions where the dichalcogenide layer reacts with Li, similar to the lithiation of silicon, have also been predicted theoretically.[16]

The lithium intercalation capacity can be found by density functional theory calculations or other theoretical methods, as it has been shown in the case of graphite (of which the intercalated phase is LiC_6)[17−20] Similarly, the capacity of conversion-type anodes has also been studied using atomistic simulations.[6,7] Some studies of Li insertion in compound layered materials have intercalation stages similar to graphite.[21−23] There are several previous studies of Li adsorption on

Received: April 29, 2024
Revised: June 27, 2024
Accepted: July 9, 2024
Published: July 24, 2024

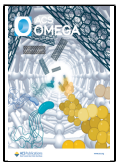

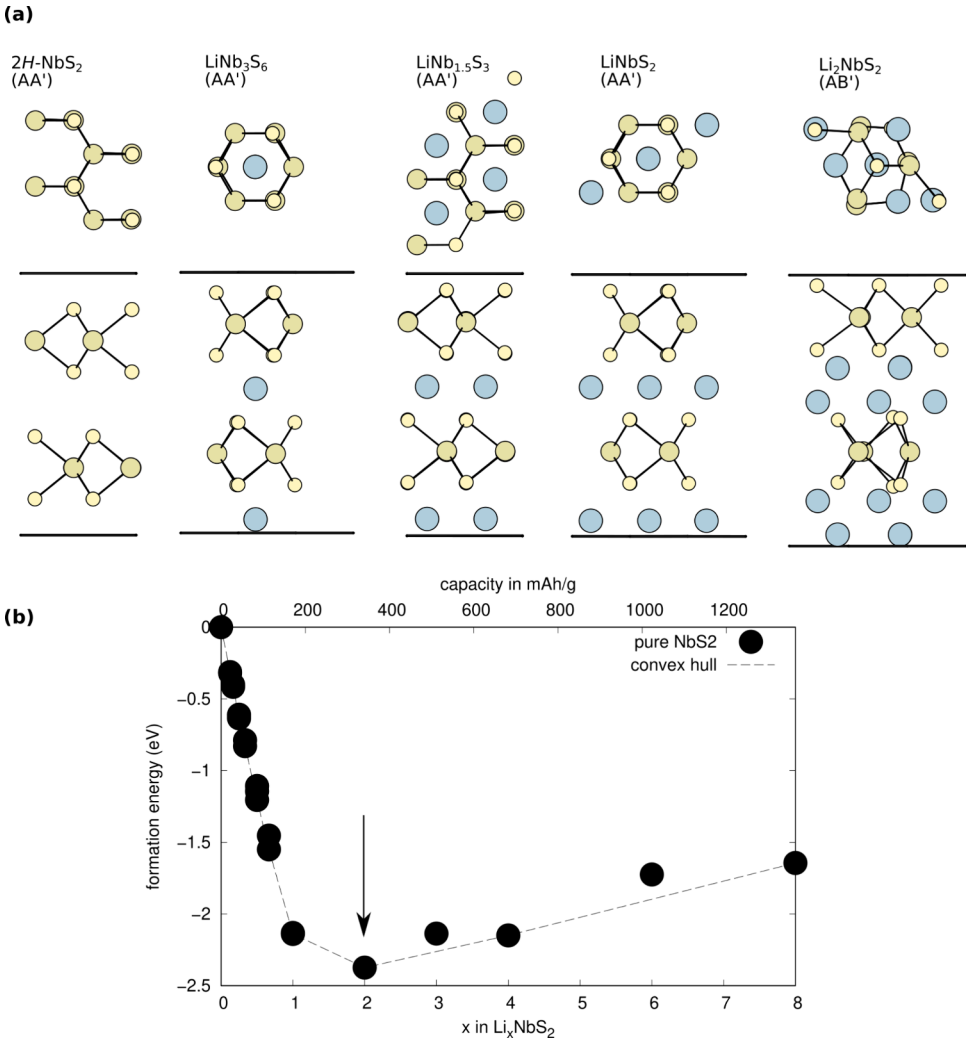

Figure 1. Structures of (a) Li-intercalated pristine NbS_2 (Li_xNbS_2) and (b) formation energy vs Li content for pristine NbS_2 (Li_xNbS_2). Nb, S and Li atoms are represented in dark yellow, light yellow, and blue, respectively. The arrow indicates the lowest formation energy, corresponding to maximum capacity.

a NbS_2 monolayer.[24−26] A previous study of bulk 2*H*-NbS_2 (which we will just refer to as NbS_2) found that its structure is largely unchanged by lithium insertion.[16] However, there is a need to understand the stages of lithiation of the bulk NbS_2 and the influence of the presence of defects on the onset of the conversion-type reactions, and the respective maximum capacity.

In this article, we show that NbS_2 is a high-capacity anode material, with two Li insertion phases: intercalation, up to 340.8 mAh/g, followed by a partially reversible conversion (alloying) phase dependent on the presence of defects, up to 1459.8 mAh/g. We propose that a double Li layer intercalation is responsible for a higher capacity of NbS_2 in pristine material. We also characterize experimentally the Galvanic charge/discharge cycling of NbS_2-based anodes in NbS_2/Li half cells, demonstrating the robustness of the high anode capacity. A comparison between theory and experiment enables us to identify the main Li insertion stages observed.

2. RESULTS AND DISCUSSION

The voltage across a battery or half cell, at a point in time when the fraction of Li in the cathode is x, is given by

$$V(x) = -\frac{\mu_{\mathrm{Li}}^{\mathrm{cathode}}(x) - \mu_{\mathrm{Li}}^{\mathrm{anode}}(x)}{F} \tag{1}$$

where $\mu_{\mathrm{Li}}^{\mathrm{cathode}}(x)$ and $\mu_{\mathrm{Li}}^{\mathrm{anode}}(x)$ are the chemical potentials of the cathode and anode, and F is the Faraday constant. An anode material is typically tested in a half-cell with a body-centered cubic (bcc) Li metal electrode, and in that case $V(x) = \left[\frac{1}{x}E(\mathrm{Li}_x\mathrm{NbS}_2) - E(\mathrm{Li\text{-}bcc})\right]/F$, where E(Li–bcc) is the energy of a Li atom at the bcc Li electrode. The maximum capacity of bulk NbS_2 and its corresponding lithiated composition Li_xNbS_2 can be identified by finding the Li content x_c for which the voltage drops to zero, $V(x_c) = 0$. Since

$$V(x_c) - V(x) = \mu(x_c) - \mu(x) = \frac{E_f(x_c) - E_f(x)}{x_c - x} \tag{2}$$

where $E_f(x)$ is the formation energy per Li atom of $E(\mathrm{Li}_x\mathrm{NbS}_2)$. thus, the lithium content at full capacity x_c can also be found by minimizing the formation energy

$$E_f(x) = E(\mathrm{Li}_x\mathrm{NbS}_2) - xE(\mathrm{Li\text{-}bcc}) - E(\mathrm{NbS}_2) \tag{3}$$

https://doi.org/10.1021/acsomega.4c04118
ACS Omega 2024, 9, 33912−33918

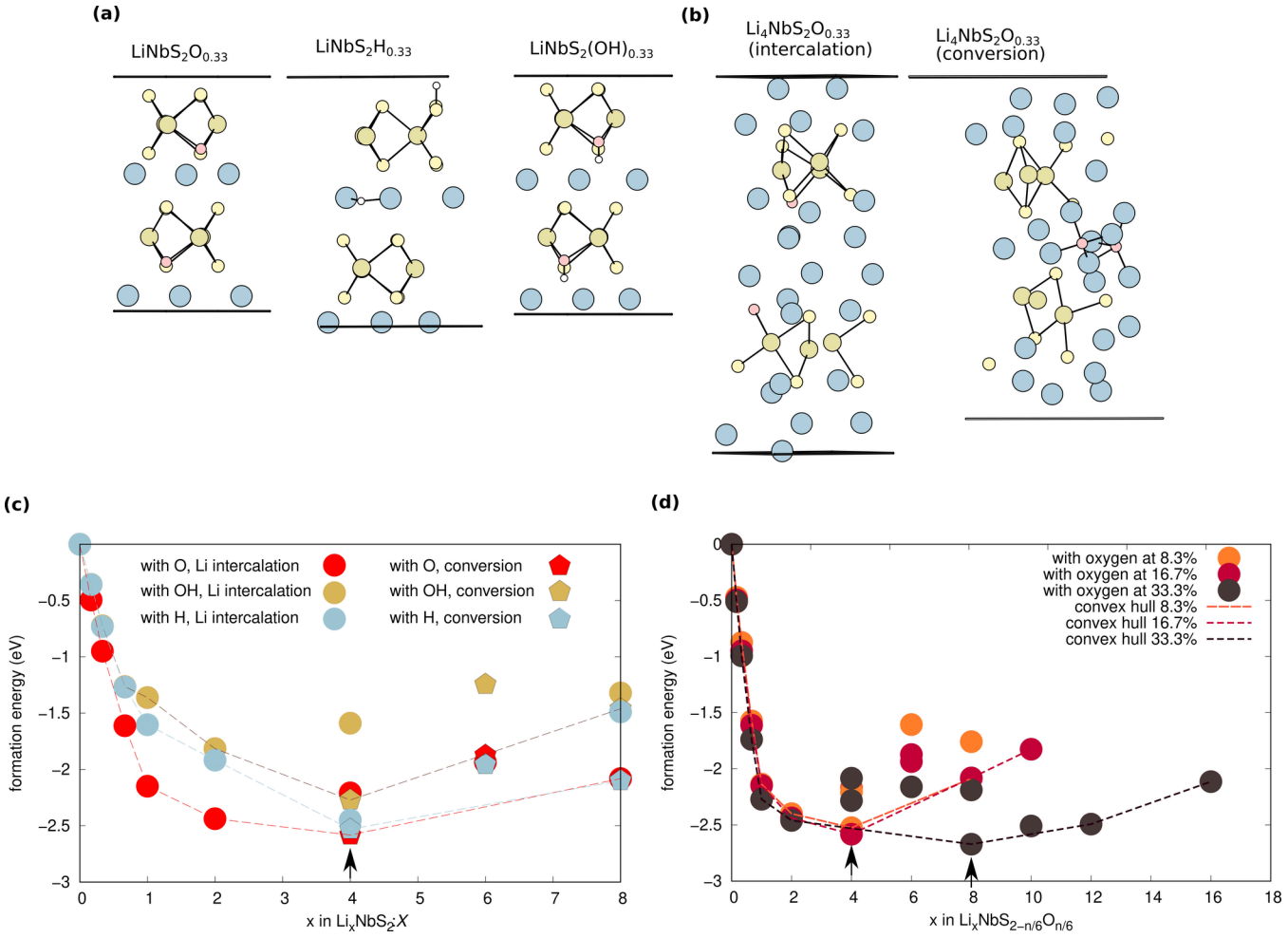

Figure 2. (a) Li-intercalated defective NbS_2 with O, OH replacing for S and/or hydrogen doping, for low Li content, and (b) intercalation vs conversion (alloying) of $Li_xNbS_{2-y}O_y$, with 2 defects per unit cell (c) energy of partially oxidized/hydrogenated lithiated NbS_2 ($Li_xNbS_{2-y}O_yH_z$), with two defects per unit cell, and (d) formation energy of partially oxidized lithiated NbS_2 ($Li_xNbS_{2-y}O_y$), as a function of the Li and O content. Percentages of defects are the percentage of S substitution. Nb, S and Li atoms are represented in dark yellow, light yellow, and blue respectively, O and H atoms in pink and white, respectively. The arrow indicates the lowest formation energy, corresponding to maximum capacity.

where $E(Li_xNbS_2)$ is the total energy per formula unit (f.u.) of the lithiated supercell and $E(NbS_2)$ is the total energy per f.u. of pristine 2*H*-NbS_2. All the energies were calculated using DFT, as detailed in the methods section.

The structure of pristine NbS_2 has AA′ stacking (for stacking nomenclature, please refer to ref 27), with the Nb atoms of one layer stacked on top of the S atoms of the neighboring layers. The hexagonal interstitial sites of all layers are aligned and therefore, in contrast to graphite, there is no change of stacking for stage I intercalation (for Li_xNbS_2 with x = 1/4, 1/3, 1/2, 2/3, 1). Some of the most important phases of Li intercalation are shown in Figure 1. For $LiNb_2S_4$, all the hexagonal sites are occupied. This is different from the intercalated graphite LiC_6 where there are no nearest-neighbor occupied hexagonal sites, and possibly is due to the increased screening of NbS_2, with a larger density of states at the Fermi level than graphite.

Notably, there is a stable phase for x = 2 corresponding to a double Li layer intercalation that is not present in graphite. For 2 > x > 1, the Li atoms start arranging themselves in double layers resembling the stacking of Li-hcp, and the NbS_2 layers prefer AB′ stacking so as to accommodate the relative shift of the Li layers. The maximum capacity of NbS_2, corresponding to the Li_2NbS_2 phase, is 340.8 mAh/g (Figure 1). This is smaller than graphene due to the larger masses of Nb and S. However, NbS_2 can accommodate 12 times more Li atoms per cell, having a volumetric capacity of 1,364.6 mAh/cm^3 (compared to 720.0 mAh/cm^3 for graphene). The Li_2NbS_2 phase is expanded by 15% and 6% along the â and ĉ directions, respectively.

Since the material used in the experiments contained oxygen and hydrogen in various fractions, we have considered the effect that such impurities may have on the capacity. Most importantly, we have found that in the presence of defects, a conversion stage follows the intercalation stages, allowing for higher Li content to be alloyed into NbS_2, but with a loss of the layered structure.

Sulfides can have sulfur vacancies due to the volatility of sulfur, and these can be filled by oxygen.[28] Oxygen has the same valency as sulfur and therefore replaces sulfur with very little lattice distortion (Figure 2a). However, oxygen is more electronegative than sulfur, forming stronger bonds with Li. Therefore, there is a competing structure where each of the oxygen atoms exchanges place with a Li, and the NbS_2 layers are significantly distorted (Figure 2b). This structure is lower in energy than the structure where the oxygen atoms are substitutional (O_S). For 16.7% oxygen concentration (1/sixth

https://doi.org/10.1021/acsomega.4c04118
ACS Omega 2024, 9, 33912−33918

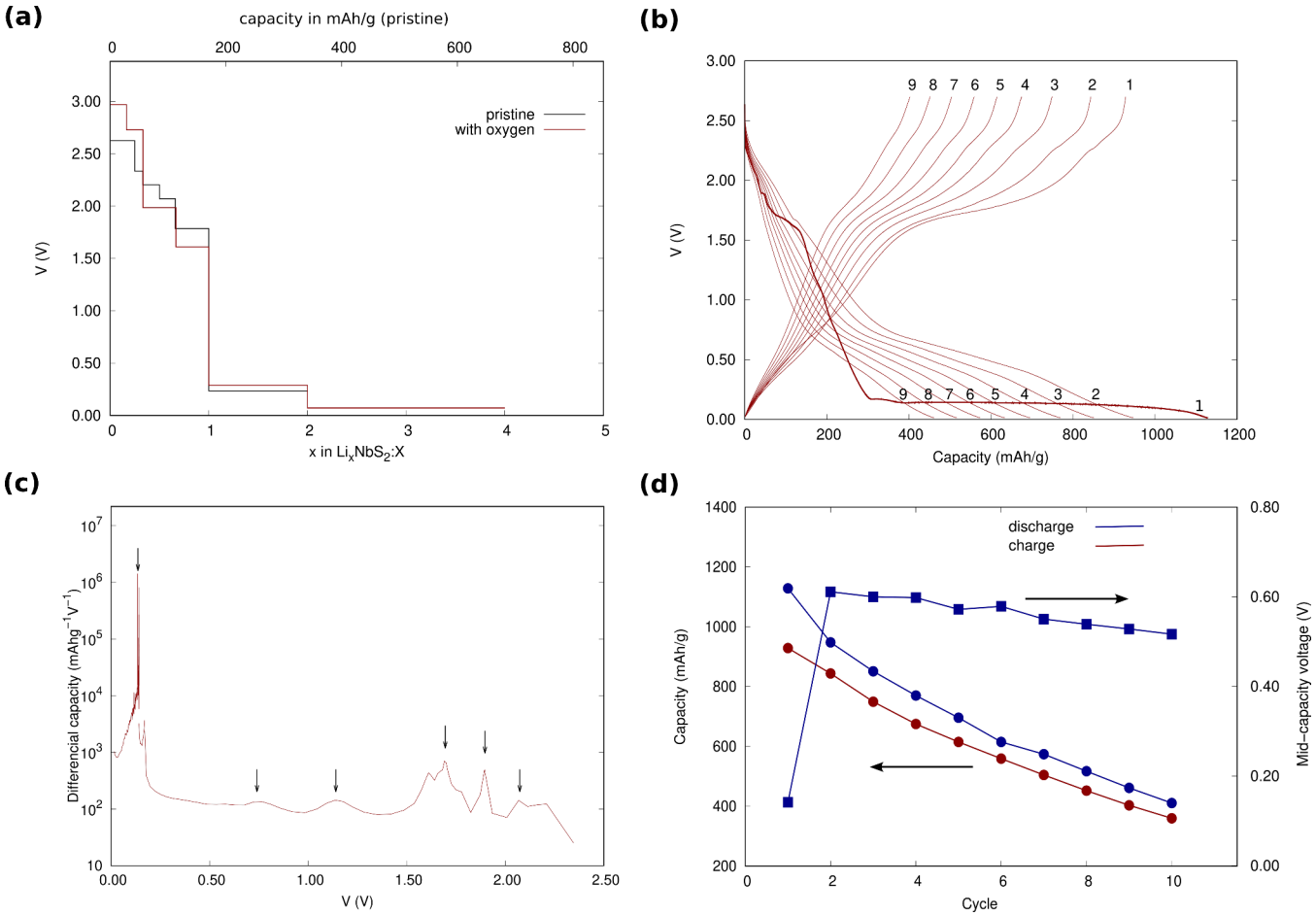

Figure 3. (a) Theoretical potential difference with respect to metallic Li; (b) experimental voltage-capacity curves for the first nine charge and discharge cycles (c) derivative of the first-cycle experimental capacity with respect to voltage and (d) degradation of the experimental charge and discharge capacities and midcapacity voltage.

of the sulfur replaced by oxygen), the energy gain is 0.37 eV/f.u. for Li_4NbS_2, bringing $x = 4$ to a lower formation energy than $x = 2$ (Figure 2-c), thus doubling the capacity.

The oxygen presence thus leads to higher lithium intake, leading to partial NbS_2 lattice breakdown, similar to what happens in Si anodes. Such conversion-type reaction has also been theoretically predicted for other transition metal chalcogenides.[16] The essential difference in the case of NbS_2 is that the presence of defects is necessary to trigger the conversion-type Li insertion for $x > 2$. The formation energies of the lithiated phases, including those that are the product of conversion-type reactions, are shown in Figure 2-b) for an oxygen content of 16%. Up to $x = 2$, the succession of phases and their formation energies are nearly unaltered (Figure 2-c). However, for $x = 4$, the intercalated phase is 0.4 eV/f.u. higher in energy than the alloyed phase obtained after the reaction of the oxygen atoms with Li, both shown in Figure 2-b. In the alloyed structure, Li atoms have taken the place of the oxygen atoms. The oxygen atoms are at the inner Li layers, connected to 8 Li atoms each, in a local environment that resembles Li_2O. The maximum intercalation capacity is doubled to 681.6 mAh/g (Figure 2-c).

As the oxygen concentration increases up to 33.3%, the minimum formation energy shifts to $x = 8$ in $Li_8NbS_{1.33}O_{0.67}$ (Figure 2-d)). The capacity for Li intake for this concentration is 1,459.8 mAh/g. The increase in capacity is also at the expense of conversion of the structure. We found that if the oxygen fraction exceeds the sulfur fraction, the hull curve becomes too deep in energy, and the conversion process can be considered irreversible at normal operating conditions.

We found that the effect of hydrogen and hydroxyl defects is similar, both triggering covalent bond breaking in the presence of large fractions of Li, and allowing the material to undergo a conversion reaction when present. A single hydrogen atom prefers to bond to the S atom, forming a sulfhydryl group. The interstitial hydrogen at the Li plane is 1.22 eV higher in energy. However, if a pair of hydrogens are present, with the first in a sulfhydryl group, the second loses its electron to the vicinity of the first sulfhydryl group, becoming an interstitial (Figure 2-a). For a hydrogen:sulfur ratio of 1:6, we find a higher capacity than for the pristine material (Figure 2-c). Similar to the case of oxygen, the maximum intercalation is at x = 4 and is accompanied by lattice disruption, with Li taking the place previously occupied by H. Hydroxyl radicals are another possible occurrence at the sulfur sites. Similar to oxygen, there is little lattice disruption for $x \leq 2$. For x = 4, there is a breakdown of the Li lattice, with Li atoms and hydroxyl units exchanging place. This also leads to higher capacity (Figure 2-c).

The voltage profile can be derived from the hull energies. The voltage drop between two lithiated phases with Li contents x_0 and x_1 is given by

https://doi.org/10.1021/acsomega.4c04118
ACS Omega 2024, 9, 33912−33918

$$V_{x_1} - V_{x_0} = G(\mathrm{NbLi}_{x_1}\mathrm{S}_2 - G(\mathrm{NbLi}_{x_0}\mathrm{S}_2)/(x_1 - x_0) \quad (4)$$

where the free energy G can be approximated by the formation energy. Setting the intercalated phase at the maximum capacity limit $x = x_{max}$ as the zero voltage, we obtain the average potential as a function of the Li intercalation content shown in Figure 3.

For transition metal oxide anodes, the generalized gradient approximation of density functional theory employed here has been found to underestimate the lithiation voltage, which can be corrected with a Hubbard-U type correction that lowers the energy of the Li electron in the transition metal d orbitals.[29] However, it not clear how to choose U and how relevant is that correction in the case of NbS_2.

To compare the calculated voltage profile with the theoretical calculations, half cells were constructed using Li-metal as the counter and reference electrodes against NbS_2-based (99.99% Niobium Disulfide, American Elements, CAS 12136−97−9) working electrodes. Celgard 2325 and Whatman GF/A were used as the separators and 1.0 M lithium hexafluorophosphate ($LiPF_6$) in ethylene carbonate and dimethyl carbonate (1.0 M $LiPF_6$ in EC/DMC 50/50 (v/v)) as the electrolyte. The working electrodes, with active material mass loading of 1.3 mg, were made using the ratio composition of 90/5/5 (NbS_2/Super-P carbon black/CMC+SBR) tape-casted on Cu foil. Galvanic charge and discharge were performed to obtain the specific average capacity of the NbS_2 and cycling performance. The studies were performed with current of 0.02 mA (C-rate of 0.05C) between 0.012 and 2.7 V.

As presented in Figure 3b, NbS_2/Li delivers an initial specific discharge capacity of around 1,130 mAh/g and a first cycling-specific capacity of about 930 mAh/g, with a Coulombic efficiency of 82.3%. From the second cycle onward, a systematic specific capacity decay of around 10% was observed from each cycle to the previous. A stable Coulombic efficiency between 87 and 89% was found after the first cycle, where was detected. We found similar electrochemical behaviors in our previous work with NbS_2-based anode materials.[30]

The experimental voltage vs capacity profile for the first cycle shows several stages with transitions at approximately 2.07, 1.89, 1.69, 1.14, 0.74, and 0.14 V. Even though it is difficult to identify specific stages, the two especially prominent stages at 1.69 and 0.14 V seem to be consistent with the theoretical phase transitions to $x = 1$ and to $x = 2$, which corresponds to the intercalation of a full Li monolayer or a full Li bilayer.

A notorious change in the discharge profile was observed between the first and second Galvanic discharges. As the cycles are repeated, the stages are less pronounced, the capacity decreases and the midcapacity voltage decreases (after the second cycle). This can be due to irreversible reactions of Li with defects, and irreversible increase of the NbS_2 interlayer distance. In the presence of impurities and defects, further reaction of Li with the NbS_2 layers may also take place, as indicated by our calculations in material containing O and/or H.

The initial measured capacity of 1,130 mAh/g exceeds the theoretical predictions. The reason for this is that the experiments were carried out with imperfect material, and not single crystals. It is known that large scale defects can lead to an increase in anode capacity, due to Li storage at voids and Li trapping at defects,[31,32] and this is a possible reason for the higher experimental capacity. A variety of disordered carbons have been reported to have significantly higher capacities than graphite,[33] and one of the reasons is the adsorption of Li on both sides of the monolayers and on the edges.[34] We have performed calculations in monolayer NbS_2, showing that the capacity is the double of the bulk capacity, due to Li bilayer adsorption on both sides (Li_4NbS_2). Thus, layer disorder and decoupling may also contribute to an increased capacity, similar to disordered graphitic anodes.

After 9 cycles, the capacity is approaching the theoretical estimate for the pristine material, which could possibly be due to the reversible charge and discharge of intercalated Li but not Li reacted with the NbS_2 layers and the impurities.

3. CONCLUSION

We have shown that NbS_2 is an anode material with a theoretical capacity up to 340.8 mAh/g in the pristine state. Further, NbS_2-based anodes are very robust in the presence of oxygen and hydrogen, which even lead to at least a 2-fold increase in capacity. The increased capacity is due to the reaction of Li with the defective NbS_2 layers and is possibly associated with irreversibility. Experimentally, the NbS_2-based anodes were found to have a capacity of 1,130 mAh/g. Two prominent stages at voltages of 1.69 and 0.14 V correspond to the formation of the $LiNbS_2$ and Li_2NbS_2 phases. At maximum capacity, NbS_2 has a volume expansion of 42% upon lithiation, which is much lower than the volume expansion of silicon ($\simeq$ 300%).[35] We suggest NbS_2 as a possible alternative to silicon additives to increase anode capacity.

4. METHODS

4.1. First-Principles Calculations. First-principles calculations were based on the framework of DFT, as implemented in the Quantum ESPRESSO package.[36] The PBE[37] exchange and correlation energy functional was used. Ultrasoft pseudopotentials[38] were used for all elements except niobium, for which a norm-conserving Troullier-Martins pseudopotential was selected.[39] We employed a plane wave basis set with kinetic energy cutoffs of 80 Ry to describe the electronic wave functions. The Brillouin zone was sampled using a Γ-centered 4 × 4 × 2 Monkhorst−Pack (MP) grid[40] for all NbS_2 supercell calculations.

AUTHOR INFORMATION

Corresponding Authors

Sergio G. Echeverrigaray − *Centre for Advanced 2D Materials, National University of Singapore, 117546, Singapore*; Email: sergio@nus.edu.sg

Alexandra Carvalho − *Institute for Functional Intelligent Materials, National University of Singapore, 117544, Singapore*; orcid.org/0000-0002-2851-1887; Email: carvalho@nus.edu.sg

Authors

Vivek Nair − *CRADLE Singapore, Hyundai Motor Innovation Center in, 649674, Singapore*

Antonio H. Castro Neto − *Centre for Advanced 2D Materials, National University of Singapore, 117546, Singapore; Department of Materials Science Engineering, National University of Singapore, 117575, Singapore; Institute for Functional Intelligent Materials, National University of Singapore, 117544, Singapore*

https://doi.org/10.1021/acsomega.4c04118
ACS Omega 2024, 9, 33912−33918

Complete contact information is available at:
https://pubs.acs.org/10.1021/acsomega.4c04118

Notes

The authors declare no competing financial interest.

■ ACKNOWLEDGMENTS

This research project is supported by the Ministry of Education, Singapore, under its Research Centre of Excellence award to the Institute for Functional Intelligent Materials, National University of Singapore (I-FIM, project No. EDUNC-33-18-279-V12). This work used computational resources of the Centre of Advanced 2D Materials (CA2DM), funded by the National Research Foundation, Prime Ministers Office, Singapore; and the Singapore National Supercomputing Centre (NSCC). We thank the financial support and contributions from Companhia Brasileira de Metalurgia e Mineração (CBMM), which made this study possible. Additionally, we appreciate the collaborative environment provided by CBMM, which significantly enhanced the quality and impact of our research.

■ REFERENCES

(1) Asenbauer, J.; Eisenmann, T.; Kuenzel, M.; Kazzazi, A.; Chen, Z.; Bresser, D. The success story of graphite as a lithium-ion anode material−fundamentals, remaining challenges, and recent developments including silicon (oxide) composites. *Sustainable Energy & Fuels* **2020**, *4*, 5387−5416.

(2) Orsini, F.; Du Pasquier, A.; Beaudoin, B.; Tarascon, J.; Trentin, M.; Langenhuizen, N.; De Beer, E.; Notten, P. In situ scanning electron microscopy (SEM) observation of interfaces within plastic lithium batteries. *J. Power Sources* **1998**, *76*, 19−29.

(3) Schmuch, R.; Wagner, R.; Hörpel, G.; Placke, T.; Winter, M. Performance and cost of materials for lithium-based rechargeable automotive batteries. *Nature energy* **2018**, *3*, 267−278.

(4) Chen, S.; Niu, C.; Lee, H.; Li, Q.; Yu, L.; Xu, W.; Zhang, J.-G.; Dufek, E. J.; Whittingham, M. S.; Meng, S.; et al. others Critical parameters for evaluating coin cells and pouch cells of rechargeable Li-metal batteries. *Joule* **2019**, *3*, 1094−1105.

(5) Liu, H.; Cheng, X.-B.; Xu, R.; Zhang, X.-Q.; Yan, C.; Huang, J.-Q.; Zhang, Q. Plating/stripping behavior of actual lithium metal anode. *Adv. Energy Mater.* **2019**, *9*, 1902254.

(6) Chan, M. K.; Wolverton, C.; Greeley, J. P. First principles simulations of the electrochemical lithiation and delithiation of faceted crystalline silicon. *J. Am. Chem. Soc.* **2012**, *134*, 14362−14374.

(7) Cubuk, E. D.; Kaxiras, E. Theory of structural transformation in lithiated amorphous silicon. *Nano Lett.* **2014**, *14*, 4065−4070.

(8) Jin, Y.; Zhu, B.; Lu, Z.; Liu, N.; Zhu, J. Challenges and recent progress in the development of Si anodes for lithium-ion battery. *Adv. Energy Mater.* **2017**, *7*, 1700715.

(9) Nitta, N.; Wu, F.; Lee, J. T.; Yushin, G. Li-ion battery materials: present and future. *Mater. Today* **2015**, *18*, 252−264.

(10) Phadatare, M.; Patil, R.; Blomquist, N.; Forsberg, S.; Örtegren, J.; Hummelgård, M.; Meshram, J.; Hernández, G.; Brandell, D.; Leifer, K.; et al. others Silicon-nanographite aerogel-based anodes for high performance lithium ion batteries. *Sci. Rep.* **2019**, *9*, 14621.

(11) Li, X.; Gu, M.; Hu, S.; Kennard, R.; Yan, P.; Chen, X.; Wang, C.; Sailor, M. J.; Zhang, J.-G.; Liu, J. Mesoporous silicon sponge as an anti-pulverization structure for high-performance lithium-ion battery anodes. *Nat. Commun.* **2014**, *5*, 4105.

(12) Liu, X. H.; Zhong, L.; Huang, S.; Mao, S. X.; Zhu, T.; Huang, J. Y. Size-dependent fracture of silicon nanoparticles during lithiation. *ACS Nano* **2012**, *6*, 1522−1531.

(13) Han, C.; Si, H.; Sang, S.; Liu, K.; Liu, H.; Wu, Q. Achieving fully reversible conversion in Si anode for lithium-ion batteries by design of pomegranate-like Si@ C structure. *Electrochim. Acta* **2021**, *389*, 138736.

(14) Blomgren, G. E. The development and future of lithium ion batteries. *J. Electrochem. Soc.* **2017**, *164*, A5019.

(15) Chen, B.; Chao, D.; Liu, E.; Jaroniec, M.; Zhao, N.; Qiao, S.-Z. Transition metal dichalcogenides for alkali metal ion batteries: engineering strategies at the atomic level. *Energy Environ. Sci.* **2020**, *13*, 1096−1131.

(16) Zhao, T.; Shu, H.; Shen, Z.; Hu, H.; Wang, J.; Chen, X. Electrochemical lithiation mechanism of two-dimensional transition-metal dichalcogenide anode materials: intercalation versus conversion reactions. *J. Phys. Chem. C* **2019**, *123*, 2139−2146.

(17) Persson, K.; Hinuma, Y.; Meng, Y. S.; Van der Ven, A.; Ceder, G. Thermodynamic and kinetic properties of the Li-graphite system from first-principles calculations. *Phys. Rev. B* **2010**, *82*, 125416.

(18) Lenchuk, O.; Adelhelm, P.; Mollenhauer, D. Comparative study of density functionals for the description of lithium-graphite intercalation compounds. *J. Comput. Chem.* **2019**, *40*, 2400−2412.

(19) Raju, M.; Ganesh, P.; Kent, P. R.; Van Duin, A. C. Reactive force field study of Li/C systems for electrical energy storage. *J. Chem. Theory Comput.* **2015**, *11*, 2156−2166.

(20) Li, Y.; Lu, Y.; Adelhelm, P.; Titirici, M.-M.; Hu, Y.-S. Intercalation chemistry of graphite: alkali metal ions and beyond. *Chem. Soc. Rev.* **2019**, *48*, 4655−4687.

(21) Liu, T.; Jin, Z.; Liu, D.-X.; Du, C.; Wang, L.; Lin, H.; Li, Y. A density functional theory study of high-performance pre-lithiated MS_2 (M= Mo, W, V) monolayers as the anode material of lithium ion batteries. *Sci. Rep.* **2020**, *10*, 6897.

(22) Xu, B.; Wang, L.; Chen, H.; Zhao, J.; Liu, G.; Wu, M. Adsorption and diffusion of lithium on 1T-MoS_2 monolayer. *Computational materials science* **2014**, *93*, 86−90.

(23) Carvalho, A.; Castro Neto, A. H. Donor and acceptor levels in semiconducting transition-metal dichalcogenides. *Phys. Rev. B* **2014**, *89*, 081406.

(24) de Rezende Neto, A. S.; Seixas, L. Toward a two-dimensional NbS2-based electrode for lithium−ion batteries. *Int. J. Quantum Chem.* **2021**, *121*, No. e26603.

(25) Zhao, J.; Yang, Y.; Katiyar, R. S.; Chen, Z. Phosphorene as a promising anchoring material for lithium−sulfur batteries: a computational study. *Journal of Materials Chemistry A* **2016**, *4*, 6124−6130.

(26) Zhu, J.; Alshareef, H. N.; Schwingenschlögl, U. Functionalized NbS2 as cathode for Li-and Na-ion batteries. *Appl. Phys. Lett.* **2017**, *111*, 043903.

(27) Tao, P.; Guo, H.-H.; Yang, T.; Zhang, Z.-D. Stacking stability of MoS_2 bilayer: An ab initio study. *Chinese Physics B* **2014**, *23*, 106801.

(28) Hu, Z.; Avila, J.; Wang, X.; Leong, J. F.; Zhang, Q.; Liu, Y.; Asensio, M. C.; Lu, J.; Carvalho, A.; Sow, C. H. others The role of oxygen atoms on excitons at the edges of monolayer WS_2. *Nano Lett.* **2019**, *19*, 4641−4650.

(29) Zhou, F.; Cococcioni, M.; Marianetti, C. A.; Morgan, D.; Ceder, G. First-principles prediction of redox potentials in transition-metal compounds with LDA+U. *Phys. Rev. B* **2004**, *70*, 235121.

(30) Nair, V.; Graniero Echeverrigaray, S.; Castro Neto, A. H. Core-shell nanoparticles and methods of fabrication thereof. International Patent Application WO2023200405A2, 2019.

(31) Wang, M.; Wang, J.; Xiao, J.; Ren, N.; Pan, B.; Chen, C.-s.; Chen, C.-h. Introducing a pseudocapacitive lithium storage mechanism into graphite by defect engineering for fast-charging lithium-ion batteries. *ACS Appl. Mater. Interfaces* **2022**, *14*, 16279−16288.

(32) Lou, S.; Cheng, X.; Gao, J.; Li, Q.; Wang, L.; Cao, Y.; Ma, Y.; Zuo, P.; Gao, Y.; Du, C.; et al. others Pseudocapacitive Li+ intercalation in porous Ti2Nb10O29 nanospheres enables ultra-fast lithium storage. *Energy Storage Mater.* **2018**, *11*, 57−66.

(33) Lim, D. G.; Kim, K.; Razdan, M.; Diaz, R.; Osswald, S.; Pol, V. G. Lithium storage in structurally tunable carbon anode derived from sustainable source. *Carbon* **2017**, *121*, 134−142.

(34) Gnanaraj, J.; Levi, M.; Levi, E.; Salitra, G.; Aurbach, D.; Fischer, J. E.; Claye, A. Comparison between the electrochemical behavior of

https://doi.org/10.1021/acsomega.4c04118
ACS Omega 2024, 9, 33912−33918

disordered carbons and graphite electrodes in connection with their structure. *J. Electrochem. Soc.* **2001**, *148*, A525.
(35) Galvez-Aranda, D. E.; Seminario, J. M. Simulations of a LiF solid electrolyte interphase cracking on silicon anodes using molecular dynamics. *J. Electrochem. Soc.* **2018**, *165*, A717.
(36) Giannozzi, P.; et al. QUANTUM ESPRESSO: A Modular and Open-Source Software Project for Quantum Simulations of Materials. *J. Phys.: Condens. Matter* **2009**, *21*, 395502.
(37) Perdew, J. P.; Burke, K.; Ernzerhof, M. Generalized Gradient Approximation Made Simple. *Phys. Rev. Lett.* **1996**, *77*, 3865.
(38) Rappe, A. M.; Rabe, K. M.; Kaxiras, E.; Joannopoulos, J. Optimized Pseudopotentials. *Phys. Rev. B* **1990**, *41*, 1227.
(39) Troullier, N.; Martins, J. L. Efficient pseudopotentials for plane-wave calculations. *Phys. Rev. B* **1991**, *43*, 1993−2006.
(40) Monkhorst, H. J.; Pack, J. D. Special Points for Brillouin-Zone Integrations. *Phys. Rev. B* **1976**, *13*, 5188.

https://doi.org/10.1021/acsomega.4c04118
ACS Omega 2024, 9, 33912−33918